Estimate microstructure development from sintering shrinkage: A kinetic field approach

Charles Manière, Thomas Grippi, Sylvain Marinel

To cite this version:

Charles Manière, Thomas Grippi, Sylvain Marinel. Estimate microstructure development from sintering shrinkage: A kinetic field approach. Materials Today Communications, 2022, 31, pp.103269. 10.1016/j.mtcomm.2022.103269 . hal-03588296

HAL Id: hal-03588296
https://cnrs.hal.science/hal-03588296v1

Submitted on 24 Feb 2022

Estimate microstructure development from sintering shrinkage: a kinetic field approach

Charles Manière[1]*, Thomas Grippi[1,2], Sylvain Marinel[1]

1 Normandie Univ, ENSICAEN, UNICAEN, CNRS, CRISMAT, 14000 Caen, France
2 Thales Alenia Space, 5 Allée des Gabians, 06150 Cannes, France

Keywords

Grain growth, Sintering trajectory, Master sintering curve, Modelling, Zirconia

Abstract

Methods such as the master sintering curve (MSC) or the kinetics method proposed by Wang and Raj (WR) are well-known techniques for determining the activation energy of sintering. However, a comprehensive sintering model also requires knowledge of porosity-dependent moduli, various constants, and grain growth behaviour. In this work, we detail a new method that allows the step-by-step identification of all the required sintering parameters. It is based on an experimental design that employs the MSC method and does not require additional tests. This work aims to estimate the grain growth behaviour during sintering from the shrinkage observed during the final stage, avoiding the use of a time-consuming interrupted-sintering study and subsequent analysis by microscopy. The grain growth behaviour was estimated by determining the densification behaviour and temperature-dependent parameters at the intermediate stage of sintering followed by determination of grain growth behaviour during the final stage based on the observed reduction in the rate of densification. The experimental MSC was incorporated into a Skorohod–Olevsky-based model, allowing the sintering behaviour to be predicted with high accuracy. This method is superior to the traditional MSC approach as it allows the sintering trajectory to be modelled and incorporates parameters that are compatible with finite element simulation.

Graphical abstract

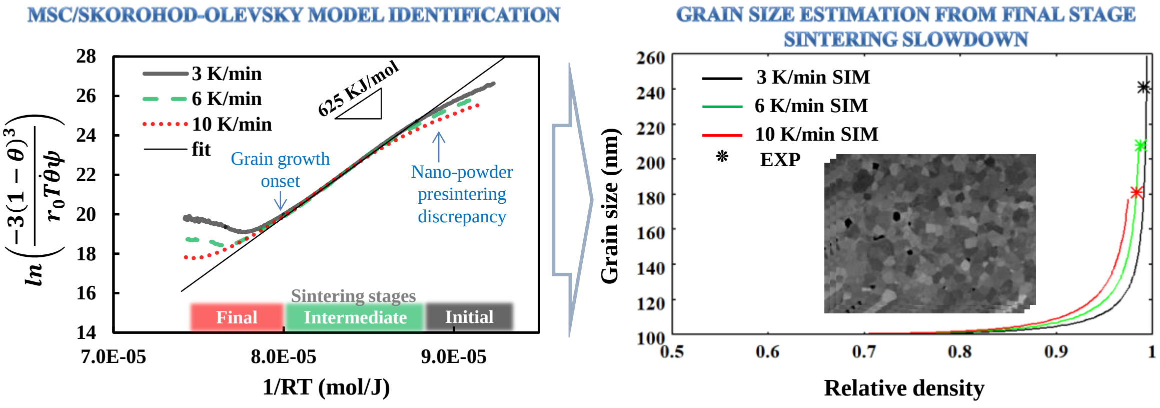

---

* Corresponding author: **CM**: Laboratoire de cristallographie et sciences des matériaux (CRISMAT), 6 Bvd du maréchal Juin 14050 CAEN CEDEX 4, France

Ph.: +33.2.31.45.13.69 ; *E-mail address*: charles.maniere@ensicaen.fr

Nomenclature

θ Porosity

$\dot{\theta}$ Porosity elimination rate (s^{-1})

$h_{t,f}$ Instantaneous or final specimen height (mm)

$\underline{\sigma}$ Stress tensor ($N.m^{-2}$)

$\underline{\dot{\varepsilon}}$ Strain rate tensor (s^{-1})

$\dot{e}$ Trace of the strain rate tensor (s^{-1})

φ Shear modulus

ψ Bulk modulus

P_l Sintering stress (Pa)

$\mathbb{I}$ Identity tensor

α Surface energy ($J.m^{-2}$)

r Mean particle radius (m)

η Material viscosity (Pa.s)

η_0 Viscosity pre-exponential factor (Pa.s)

Q Viscosity activation energy ($J.mol^{-1}$)

R Gas constant 8.314 ($J.mol^{-1}.K^{-1}$)

T Temperature (K)

$\dot{G}$ Grain growth rate ($m.s^{-1}$)

G Grain size diameter (m)

G_0 Initial grain size diameter (m)

p Grain growth rate exponent

K Grain growth factor ($m^{1+p}.s^{-1}$)

k_0 Grain growth pre-exponential factor ($m^{1+p}.s^{-1}$)

Q_G Grain growth activation energy ($J.mol^{-1}$)

m Viscosity grain size exponent

C_0 Constant

Ω Atomic volume (m^3)

k Boltzmann constant ($J.K^{-1}$)

D Diffusion coefficient ($m^2.s^{-1}$)

w Sintering equation grain size exponent

$\Gamma(\theta)$ Sintering model porosity function

1. Introduction

Establishing a comprehensive model of pressureless sintering is a challenge that requires consideration of numerous coupled phenomena such as the porosity and temperature dependence of the densification kinetics, grain growth during the final stage, the coarsening phenomenon, and microstructure development[1,2]. Various diffusional models have been developed[3,4] to predict the microstructural evolution during the initial (particle contact)[5], intermediate (cylindrical pores formation), and final stages (isolated pores formation) of sintering[6,7]. The combined-stage theory[8] provides the possibility of modelling the dissimilar geometrical parameters of all sintering stages by employing a unique porosity-dependent function, in accordance with the model proposed by Wang and Raj (WR) [9]. The WR model is employed to identify the sintering mechanism and the activation energy. Among the existing approaches, constant heating-rate methods such as the formation of master sintering curves (MSC)[10] and use of the WR method [9] are widespread. Contrary to older direct regression methods[11], these two methods allow an estimation of the activation energy to be made without disturbances from the unknown porosity function. For the MSC method, the impact of the final stage grain growth is partially taken into account under the assumption of a unique sintering trajectory $G(\rho)$. However, discrepancies can occur for materials with dissimilar trajectories; hence, Park *et al.* [12,13] modified the initial formulation to include grain growth independently. We experimentally tested this formulation on $MgAl_2O_4$; however, only a small difference in activation energy was observed[14]. The WR model needs to be applied at constant porosity and grain size; its main advantage over the MSC method is its capability of estimating the activation energy in a very narrow porosity/temperature domain[15]. Materials that exhibit phase changes or abrupt changes in the sintering mechanism can be easily characterised using this method. Nevertheless, unconventional MSC methods can also be applied in different sintering zones[16,17].

Predicting the sintering response of a powder is a challenging process, as one needs to identify (i) the temperature-dependent behaviour using the MSC and/or WR methods, (ii) the porosity-dependent behaviour [18,19] which is represented by the bulk modulus and Laplace sintering stress expression[19,20], and (iii) the grain growth behaviour[22]. Independent determination of grain growth behaviour and the bulk modulus requires a more in-depth study (i.e., interrupted isothermal sintering tests)[23]. Direct regression methods have been developed to identify densification behaviour using theoretical-porosity functions[11,24–26]. The main issue with these "direct" approaches is the influence that the theoretical porosity behaviour has on the identified mechanism. Combining such a direct method with the MSC method would allow independent determination of the activation energy and other sintering parameters without the influence of the porosity function. In this study, the MSC-derived activation energy was incorporated into the direct method regression to calibrate the porosity function and determine the pre-exponential constant at the intermediate stage of sintering. Once the densification behaviour was determined, grain growth was estimated from the kinetic drop, which is observed during the final stage of sintering. A similar estimation of the grain size was made from this kinetic drop and applied to "Zpex Smile" zirconia powder, assuming an impact on capillarity stress [27], to predict optimal sintering trajectory[28], and to alumina [29] to model spark plasma sintering. The novel method proposed in this study allows all parameters required to model the sintering trajectories to be identified and considers the grain size influence on both capillarity forces and diffusional creep[28]. Special care was taken to formulate the model based on the continuum theory of sintering to allow finite element simulation[20,30]; finally, the analytical model equation was compared to the traditional solid-state model mentioned earlier[3].

In the following section, the formulation of the sintering model and parameter identification equation was described. Then, the methods and the experimental design were explained. Finally, the successive determination of activation energy, porosity function, and grain growth were discussed. The obtained sintering model was compared to the experimentally obtained densities and microstructures.

2. Theory and calculations

The continuum theory of sintering [20] describes the pressureless sintering of a compressible material *via* the following general equation relating the stress and strain rate tensors:

$$\underline{\sigma} = 2\eta\left(\varphi\underline{\dot{\varepsilon}} + \left(\psi - \frac{1}{3}\varphi\right)\dot{e}\mathbb{1}\right) + P_l\mathbb{1} \qquad (1)$$

where the volume shrinkage rate invariant and Skorohod’s sintering stress expression [21] are defined by:

$$\dot{e} = \dot{\varepsilon}_x + \dot{\varepsilon}_y + \dot{\varepsilon}_z \qquad (2)$$

$$P_l = \frac{3\alpha}{r}(1-\theta)^2 \qquad (3).$$

The aforementioned equations show the linear viscous sintering deformation behaviour. The mass conservation equation was employed to relate the porosity elimination rate and volume change rate and is given by:

$$\frac{\dot{\theta}}{1-\theta} = \dot{\varepsilon}_x + \dot{\varepsilon}_y + \dot{\varepsilon}_z \qquad (4)$$

For pressureless and isotropic sintering, Equations (1–4) can be formulated analytically to describe the sintering response by [20]:

$$\dot{\theta} = \frac{-P_l(1-\theta)}{2\eta\psi} \qquad (5).$$

Equation (5) can analytically model the sintering densification. However, the final stage grain growth must be considered, as it influences the sintering stress (3) and the diffusional viscosity by extending the diffusion distances. The grain growth can be modelled by the following rate equation [3,4,31]:

$$\dot{G} = \frac{K}{G^p} = \frac{k_0}{G^p} exp\left(\frac{-Q_G}{RT}\right) \qquad (6).$$

The impact of grain size on linear diffusional creep mechanisms can be calculated by considering the dependence on viscosity, temperature, and grain size, [22,29,32,33] as given by the following expression:

$$2\eta = \left(\frac{G}{G_0}\right)^m \eta_0 T \exp(\frac{Q}{RT}) \qquad (7)$$

where m = 3 for grain-boundary-diffusion creep and m = 2 for lattice-diffusion creep. Assuming an effective particle size that is close to the average grain size, it is possible to obtain an analytical sintering model considering the effect of grain size on the sintering stress and diffusional creep[28]. The following equation is obtained by coupling Equations (3) and (7) with Equation (5).

$$\dot{\theta} = \frac{-6\alpha(1-\theta)^3}{G^{m+1}\frac{\eta_0}{G_0^m} T \exp(\frac{Q}{RT})\psi} \qquad (8)$$

It is possible to combine the constants and porosity functions to obtain the typical solid-state equation described by Wang and Raj[9] and that in the combined-stage theory [8].

$$\dot{\theta} = \frac{-3\alpha\Omega D(T)}{G^w kT}\Gamma(\theta) = \frac{-C_0 \exp(\frac{-Q}{RT})}{G^w T}\Gamma(\theta) \qquad (9)$$

Comparing (8) with (9), we have: $\Gamma(\theta) = \frac{(1-\theta)^3}{\psi}$; $C_0 = \frac{6\alpha G_0^m}{\eta_0}$; $w = m + 1$.

where w = 4 for grain boundary diffusion mechanism and w = 3 for lattice diffusion.

The temperature-dependent behaviour of densification (i.e., Q and $\frac{\eta_0}{\alpha}$) can be determined in the limited grain growth zone (i.e., the intermediate stage sintering). In the latter zone and still that the particle radius is close to the grain radius, we have $G \approx G_0 \approx 2r_0$. The following regression can thus be performed.

$$Y = ln\left(\frac{-3(1-\theta)^3}{r_0 T\dot{\theta}\psi}\right) = ln\left(\frac{\eta_0}{\alpha}\right) + \frac{Q}{RT} \qquad (10)$$

At the final stage of sintering, active grain growth influences densification through the variation in diffusion distances $\left(\frac{G}{G_0}\right)^m$ and through the capillarity forces (P_l). Consequently, the sintering model, neglects the grain growth in the intermediate stage Equation (10) and the equivalent model tends to full densification[28]; at this point, it should be replaced by Equation (9). If the temperature-dependent parameters of the dense phase ($Q, \frac{\eta_0}{\alpha}$) and the porosity function $\Gamma(\theta)$ are assumed to be similar at the final stage of sintering, it is possible to estimate the grain size evolution directly from the dilatometry data *via* two different sintering mechanisms: (i) grain-boundary diffusion ($w = 4$), or (ii) lattice-diffusion ($w = 3$). The following equation is employed to estimate grain size evolution, using experimentally-derived values for θ, $\dot{\theta}$, T, the Skorohod ψ function, and the previously identified values for Q and $\frac{\eta_0}{\alpha}$.

$$G = \left(\frac{-C_0 \exp(\frac{-Q}{RT})}{\dot{\theta}T} \Gamma(\theta)\right)^{\frac{1}{w}} \qquad (11)$$

Incorporating the expressions for C_0 and $\Gamma(\theta)$, the following is obtained:

$$G = \left(\frac{-\frac{6\alpha G_0^{W-1}}{\eta_0} \exp(\frac{-Q}{RT})}{\dot{\theta}T} \frac{(1-\theta)^3}{\psi}\right)^{\frac{1}{w}} \qquad (12).$$

3. Experiment and method

3.1. Materials and characterizations

In this study, Tosoh TZ-3Y-BE zirconia (3 mol% Y_2O_3; average particle size: 40 nm) powder specimens prepared as 6 mm diameter pellets by uniaxial die pressing under 1 t. To conduct the MSC study, three dilatometry tests were performed at 3, 6, and 10 K/min to 1620 K using the thermomechanical analysis system Setsys 16/18 (SETARAM, France). The final relative density was measured using the Archimedes method. The relative density curve was calculated from the final stage density and the recorded specimen height h_t evolution assuming an isotropic behaviour $1-\theta_t=(1-\theta_f)(h_f/h_t)^3$. The final specimen microstructure was characterised by SEM microscopy (Jeol 7200 LV). The average grain size was determined by the linear intercept method (6 lines by images and on different images, 3 lines on the image width and 3 lines on the image height) using the 1.56 stereological factor [34]. To validate the model grain size prediction, SEM images were also prepared using interrupted sintering tests in a tube furnace at 442, 1148, 1288, 1382, 1493, and 1573 K at a temperature raise of 3 K/min.

3.2. Method

The identification of the sintering model parameters was carried out in four steps.

First, the identification of the sintering activation energy Q is performed by the MSC and confirmed by the WR method where the activation energy is calculated at a fixed porosity. Both MSC and WR methods may converge to the same result, except when important changes in the sintering mechanism, densification regime, phase or when very dissimilar sintering trajectories occurs [14,15].

After the sintering activation energy is determined, the densification behaviour is identified in step 2. The specific parameters that are identified in this step are the constant ratio $\frac{\eta_0}{\alpha}$ and the bulk modulus $\psi(\theta)$. The constant ratio can be identified by linear regression at the intermediate stage of sintering based on Equation (10). However, the bulk modulus function may influence the regression curve, resulting in a different activation energy than that obtained by the MSC method. Skorohod's theoretical bulk modulus has the following form[20,21]:

$$\psi=\frac{2}{3}\frac{(1-\theta)^3}{\theta} \tag{13}$$

However, this modulus does not consider the initial sintering stage when high reactivity is observed owing to the point-like contact between particles. Abouaf [35] proposed that this could be modelled using an initial stage critical-porosity parameter (θ_{ci}). We previously [36] showed that a final stage critical-porosity parameter (θ_{cf}) may also be employed for sintered materials containing large, inactive pores. Figure 1 represents Skorohod's modulus with the corrected critical porosities, which are given by the following equation.

$$\psi = \frac{2}{3}\frac{(\theta_{ci}-\theta)^3}{(\theta-\theta_{cf})} \qquad (14)$$

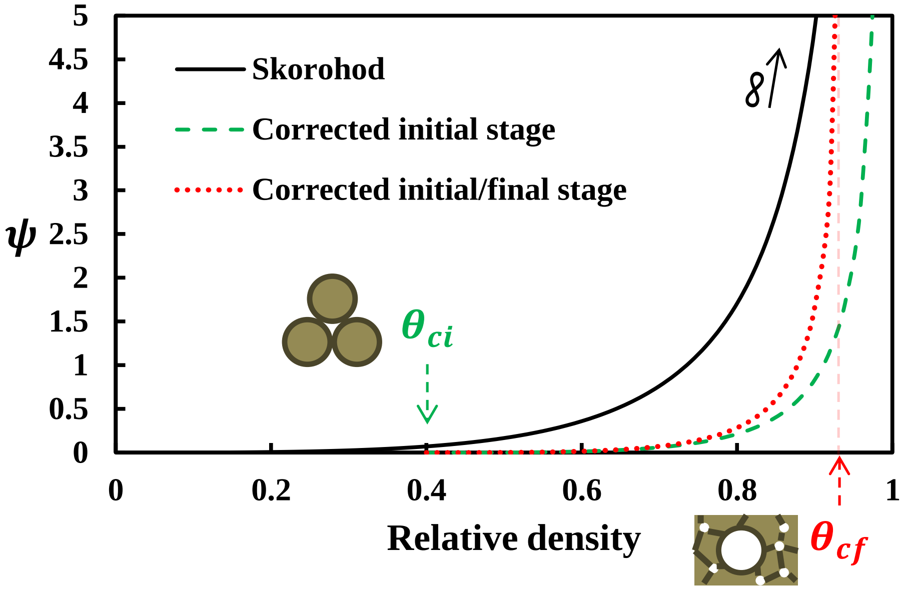

Figure 1 Skorohod's bulk modulus (black) and corrected moduli including initial stage critical porosity (green curve) and both initial, final stages critical porosities (red curve).

In this study, θ_{cf} was zero due to the high compaction and purity of the Tosoh zirconia powder which avoid the formation of macro-porosity and ensure full densification by pressureless sintering of cold-pressed powders[37]. The regression method of step 2 consists of adjusting θ_{ci} to a value slightly higher than the initial porosity and gives an activation energy (i.e., the slope at the intermediate stage) equal to that produced by the MSC and WR methods. The origin of the curve is the logarithm of the ratio $\frac{\eta_0}{\alpha}$. Step 2, therefore, is required to adjust the bulk modulus so that the activation energy matches that determined independently from the porosity function *via* the MSC method and to identify all the pre-exponential constants used in the model.

At this stage, it was possible to model sintering without grain growth. Using equation (12), an estimation of the grain size evolution in the final stage can be conducted using the identified model parameters and experimental porosity data (step 3). The two diffusional mechanisms that need to be considered are grain boundary diffusion ($w = 4$) and lattice diffusion ($w = 3$), giving two different grain size curves.

Step 4 consists of identifying the grain growth behaviour from the estimated curve and modelling the sintering trajectories based on experimental data.

3.3. Validity domain of the approach

Equation (12) estimates the grain growth from the densification curves. When approaching the theoretical density, we have $\dot{\theta} \rightarrow 0$, $\psi \rightarrow \infty$ and equation (12) is out of its inherent validity range. At this point, a typical grain growth study based on interrupted sintering cycles must be performed to continue studying the grain growth at higher temperatures. To estimate this limit, the experimental/calculated final grain sizes must be compared. The present indirect method is very effective to explore the grain growth at low temperature and high porosity conditions where obtaining polished SEM images is difficult. This method is also very effective for the ceramics having strong interactions of their densification with the grain growth. Equation (12) is not restrained to constant heating rate tests, after identifying all the densification parameters (step 1 & 2) any type heating schedule may be employed to test the grain size estimation curves.

4. Results and discussions

4.1. Activation energy identification

The relative density curves of the MSC study are shown in Figure 2. As expected, a higher level of densification was observed for slower heating rates because of the longer overall time spent at high temperatures. For each of these densification curves, the Θ parameter was calculated by,

$$\Theta = \int_0^t \frac{exp\left(\frac{-Q}{RT}\right)}{T} dt \qquad (15).$$

To determine the activation energy, a minimisation procedure was carried out according to the MSC method[10].

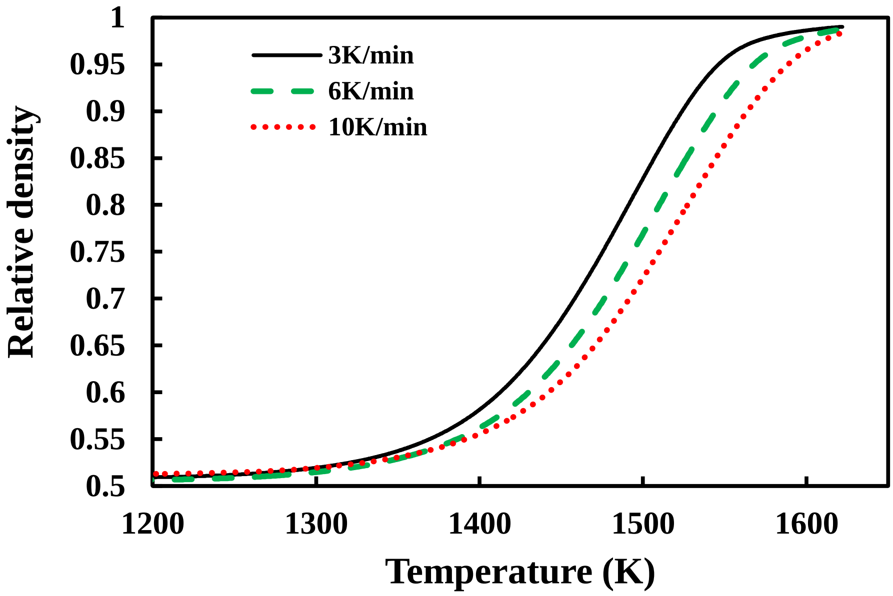

Figure 2 Relative density curves at constant heating rate of 3, 6 and 10 K/min.

The results of the MSC study are reported in Figure 3a, an activation energy of 625 kJ/mol was determined. Each curve had a good fit to the data points. A wide variety of activation energy values have been measured for 3Y-ZrO_2 powder in the literature, the value obtained in this study lies between the lower range of values (485[38], 530[39], 550 kJ/mol[40]) and the upper range of values (990[41] and 1270 kJ/mol[42]). Yamalaç et al.[39] reported a high variation in activation energy with relative density using the WR approach for this material, which could explain the wide variation in the literature values. The WR method was carried out to determine the convergence with the MSC value or the presence of an eventual variation in activation energy at different relative density. A constant value of 614 kJ/mol (close to that obtained by the MSC method, 625 kJ/mol) was measured in the relative-density range of 60–85% (Figure 3b). No significant variation in this value was observed, contrary to the findings of Yamalaç et al. [39], which may have resulted from the range of heating rates (1–10 K/min) being too large where pore coarsening by surface diffusion may occurred at the slowest heating rate [9].

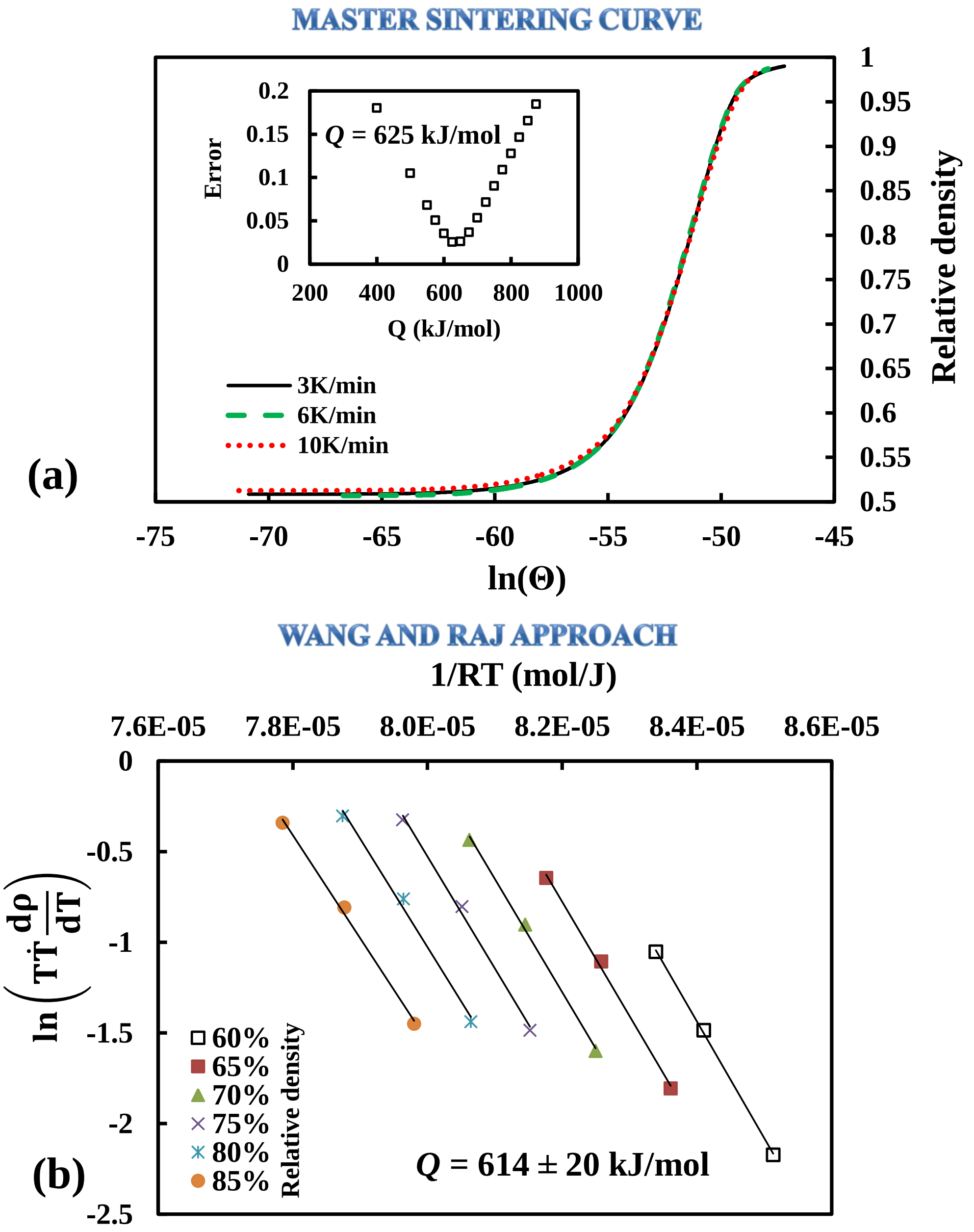

Figure 3 Sintering activation energy identification via the master sintering curve (a) and the method developed by Wang and Raj (b).

4.2. Sintering model identification

Using the activation energy determined by the MSC study, the direct regression method of step 2 can be employed to identify the ratio $\frac{\eta_0}{\alpha}$ *via* Equation (10). As mentioned earlier, the bulk modulus may influence the outcome of Equation (10), implying an error in the activation energy found by the direct method. The bulk modulus must be adjusted *via* θ_{ci}, a value slightly higher than the initial porosity, in order to obtain the same activation energy as that of the MSC method (i.e., the slope at intermediate stage). Figure 4a shows the results of the direct regression method. The adjustment of the bulk modulus for the critical porosity during the initial stage is given in Figure 4b. In the linear regression, two phenomena are apparent: (i) at the final stage of sintering, grain growth caused a deviation from the linear trend (estimation of grain size was based on this deviation) and (ii) in the initial stage, a second deviation was observed. Based on the studies by Tajiri and Al-Qureshi and Majidi et al.[43,44], highly reactive nanoparticles (40 nm) lead to presintering of the powder. It was found that the microstructure at the sintering onset (1350 K) consists of grains of approximately 96 nm. In the present study, an analysis of grain size based on an interrupted sintering cycle performed at 3 K/min was carried out, the results of which are reported in Table 1. Between 1350 K and 1500 K, the grain size stabilised to values close to 100 nm. During analytical modelling of the sintering curves (Figure 4c) using the identified ψ, Q, and $\frac{\eta_0}{\alpha}$ values, no significant deviation in grain size at the initial stage was observed because the nanoparticle presintering phenomenon implies an almost complete lack of densification. Consequently, sintering was modelled after the presintering phenomenon to avoid the differences in presintering and sintering behaviours. Therefore, the initial condition used in Equation (10) was G_0 = 100 nm.

Table 1 Interrupted sintering grain growth study at 3 K/min

Temperature (K)	442	1148	1288	1382	1493	1573

Average grain size (nm)	42.2	51.7	65.2	94.3	108.8	168.2

The analytical sintering model highlights the importance of grain growth at the final stage. This model, which neglects the grain growth at the final stage phenomenon, is unable to predict the reduction in the sintering kinetics of the final stage which is responsible for higher experimentally-determined porosities. The issue, however, can be addressed by considering grain growth.

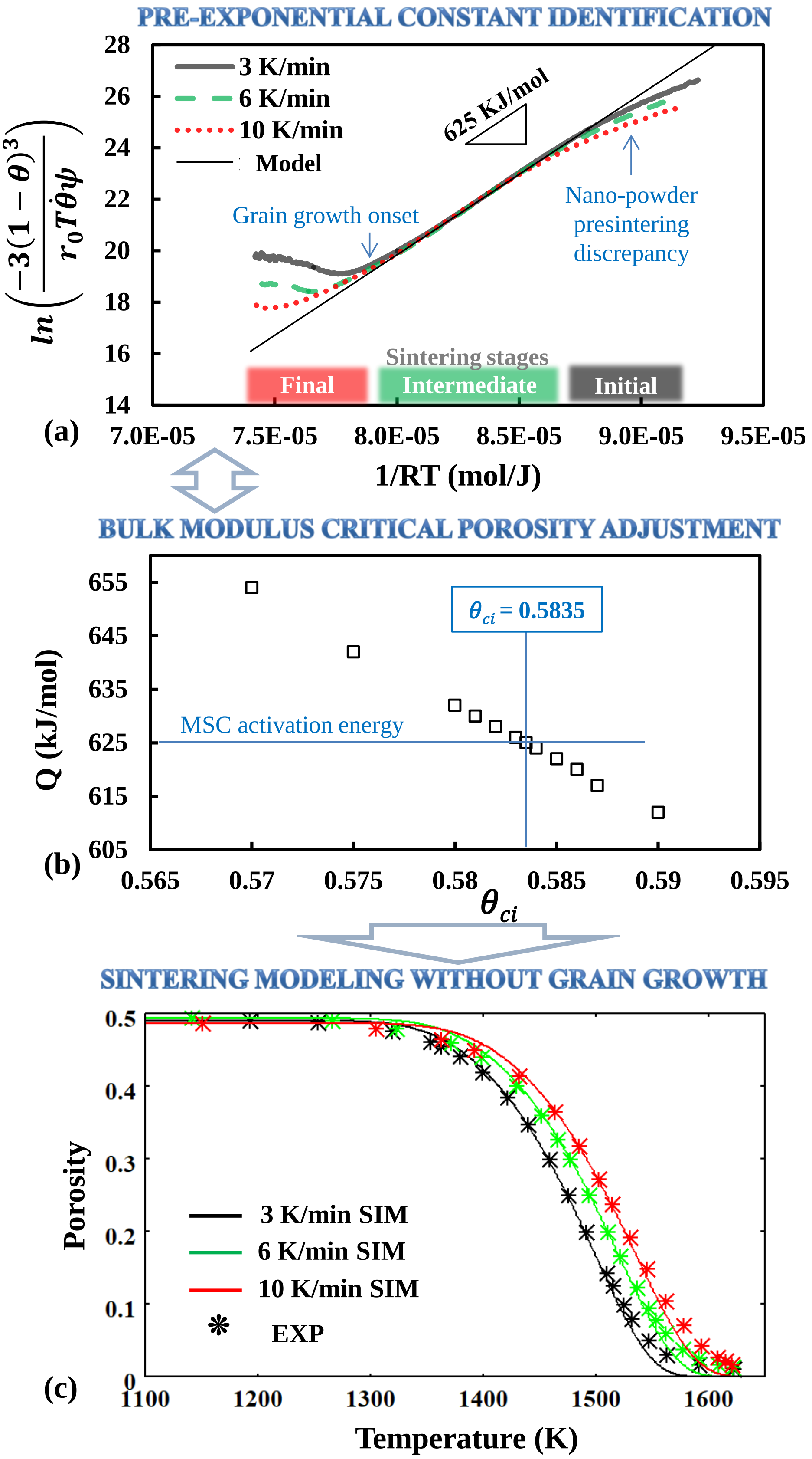

Figure 4 Modelling of the intermediate stage of sintering by direct regression using the MSC-derived activation energy (a); adjustment of the bulk modulus by critical porosity of the initial stage (b); analytical modelling of the porosity without grain growth (c); see electronic version for the colour artwork.

4.3. Grain size estimation

The sintering parameters (ψ, Q, and $\frac{\eta_0}{\alpha}$) required to calculate grain size evolution via Equation (12) were determined. For each heating rate, two grain size curves were constructed for the grain-boundary and lattice-diffusion mechanisms; w = 4 and w = 3, respectively. To compare the six curves produced with the final experimental grain size, polished microstructures were measured (Figure 5). The values of the interrupted sintering study shown in Table 1 were compared with the values predicted by the model. Equation (12) estimates grain size as a whole cycle. However, as the parameters ψ, Q, and $\frac{\eta_0}{\alpha}$ were identified with G_0 = 100 nm in Equation (10), the same grain size reference point must be considered in Equation (12). The latter estimates grain size from the deviations from linearity in the model during the initial and final stages, as shown in Figure 4a.

The change in grain size modelled at different heating rates is shown in Figure 6. The grain sizes estimated from the model match the values of the interrupted experiment well for all sintering stages. The most likely mechanism is grain–boundary diffusion because the model based on lattice diffusion predicts a final grain size that is extremely high at 3 K/min. For heating rates of 6 K/min and 10 K/min, the values predicted using the model based on the lattice diffusion mechanism appears to be more consistent with the experimental values. The differences between the two cases, however, were relatively small. Grain size as measured via the interrupted experiments confirms the modelled behaviour during the initial stage and at higher temperatures; however, this method of grain size estimation can be applied without these experimental points. Ceramics with an initial grain size >100 nm may not undergo nanograin presintering experimentally, and G_0 typically corresponds to the initial powder particle size. It is also possible to run an MSC approach and simply compare the final grain size with the predicted one.

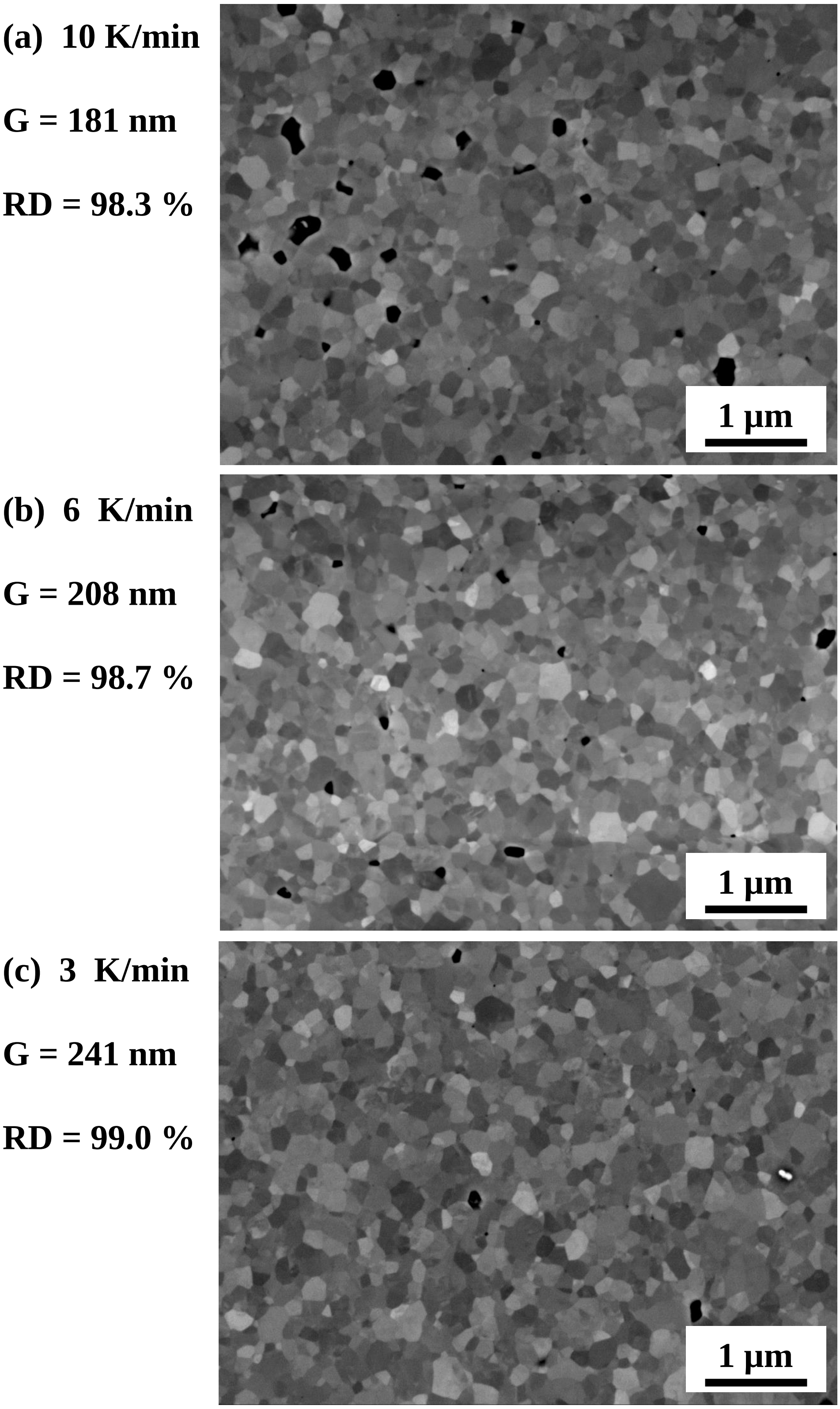

Figure 5 Final microstructures of samples sintered at 10 K/min (a), 6 K/min (b), 3 K/min (c).

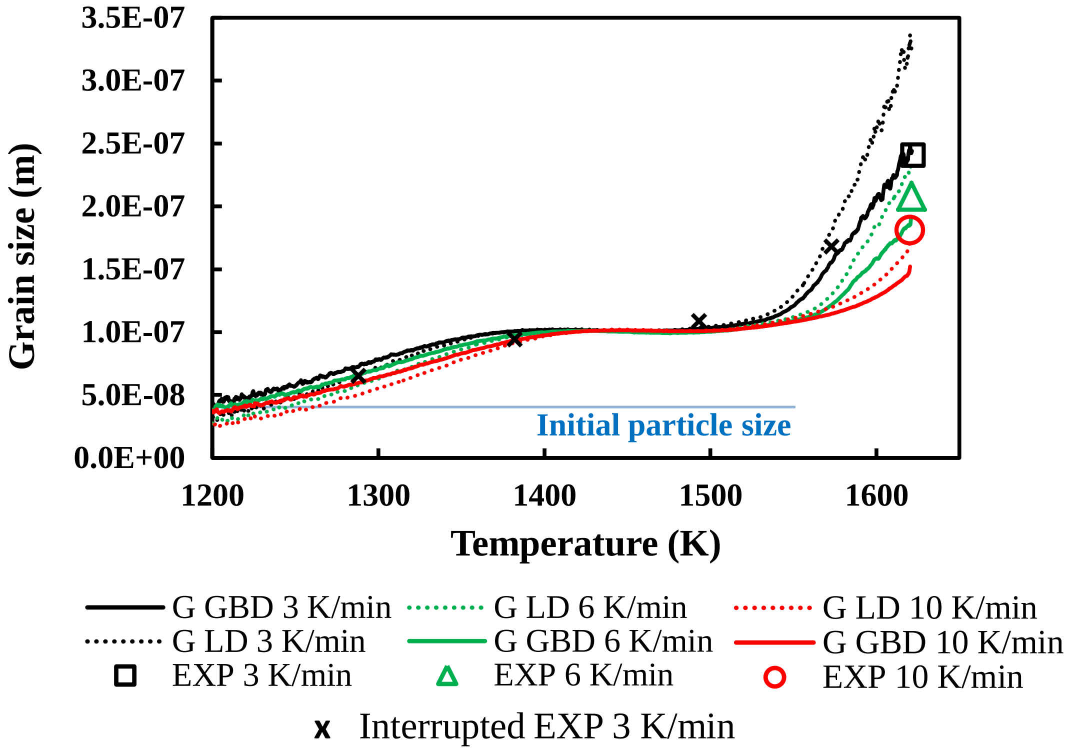

Figure 6 Estimated grain size as a function of temperature. G LD refers to the grain size curve corresponding to a lattice-diffusion mechanism, and G GBD refers to that corresponding to a grain–boundary-diffusion mechanism; see electronic version for the colour artwork.

4.4. Sintering trajectory modelling

Based on the estimated grain-size curves shown in Figure 6b and the experimental densification data shown in Figure 2, the sintering trajectories were estimated (Figure 7a). Despite the small discrepancies for 6 K/min and 10 K/min seen in Figure 6b, the sintering trajectory curves were almost aligned and correspond with the experimental data. Even the curve calculated at 3 K/min using the lattice diffusion mechanism that displayed a large deviation from the experimental value in the final grain size was consistent with the unique sintering path represented by all the curves collectively.

Identification of the transient growth law was required to analytically model the sintering trajectory by correcting the sintering model shown in Figure 4c. Equation (6) was used to model grain growth. Based on previous work [28,45], the grain growth mechanism was assumed to be a lattice-diffusion-controlled mechanism (with $p = 2$ [4]). If this method is applied to an unknown ceramic, different p exponents can be considered, for instance surface diffusion (p = 3) can be observed for grain growth under high porosity[23]. A regression method was employed to identify the grain growth activation energy Q_G and the constant k_0.

$$\ln\left(\dot{G}G^2\right) = \ln(k_0) - \frac{Q_G}{RT} \qquad (16)$$

The regression shown in Figure 7b was conducted based on the grain-size curve calculated at 3 K/min *via* the grain boundary diffusion mechanism (the black curve in Figure 6). This curve matches the experimental grain size value of the initial, intermediate, and final stages and accurately predicts the final microstructure (Figure 7a). The activation energy and k_0 values were identified as 939 kJ/mol and 21E6 m^3s^{-1}, respectively. In the literature, activation energy values of 546[46], 600[28] , 460 kJ/mol[47] were obtained for 3YTZ zirconia. Here the higher value seems to be explained by the small grain size range of the explored regions 100-200nm compared to the literature data generally close to the micron range with hours of holding. This suggests weaker grain growth kinetics near the onset, a region which is difficult to explore by conventional methods due to the concomitant densification.

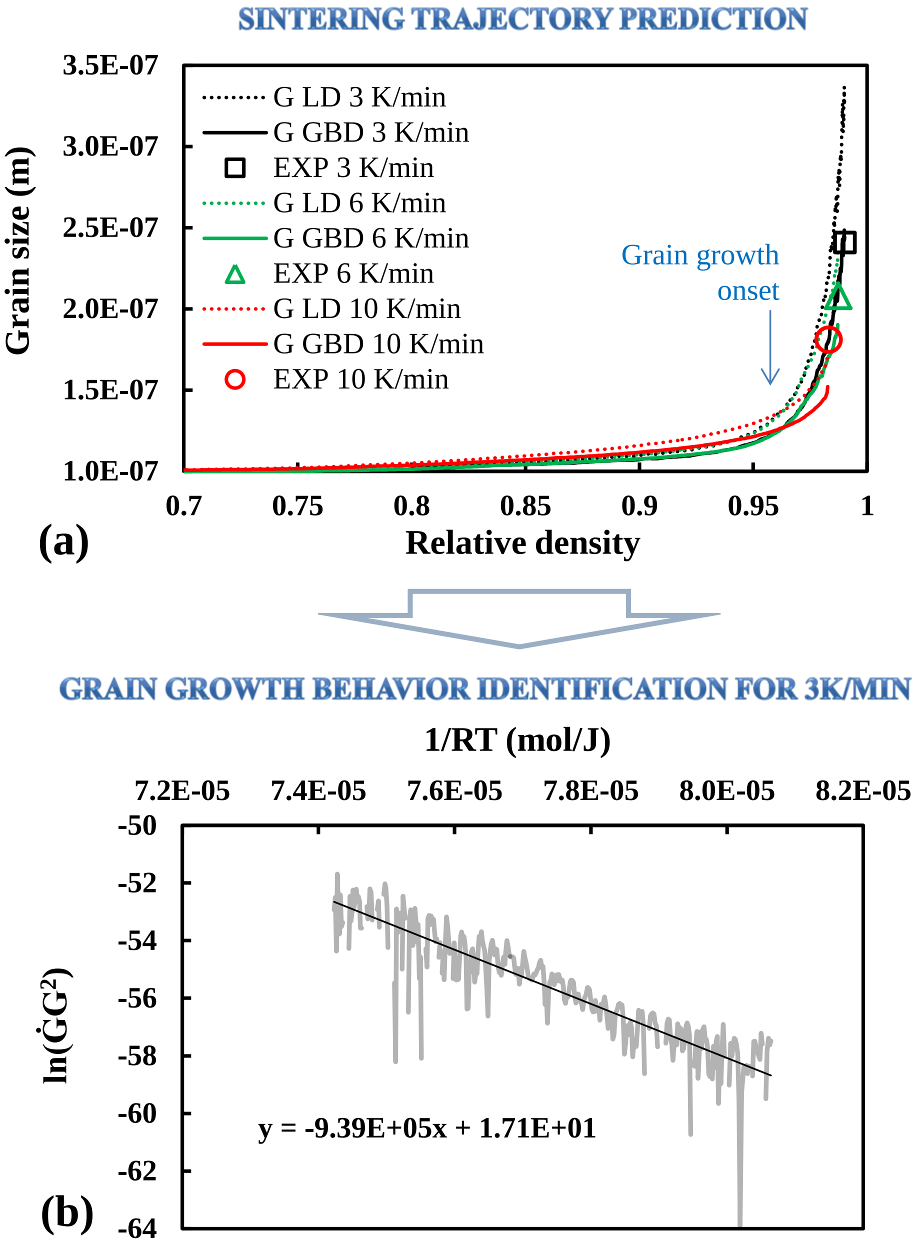

Figure 7 Predicted sintering trajectories based on estimated grain-size curves (a), identification of grain growth model based on the 3 K/min grain-boundary-diffusion-controlled sintering trajectory curve (b) ; see electronic version for the colour artwork.

The analytical sintering-trajectory model is shown in Figure 8. The porosity curves (Figure 8a) were a good fit for the entirety of the sintering process. In comparison to the model without grain growth (Figure 4c), the analytical model was able to better predict the final experimental porosities. Considering grain growth corrects the modelled behaviour of the final stage of sintering. As in the previous model, the slight presintering densification is not considered because the grain growth model (Figure 7b) focuses on the final-stage phenomenon, and the model starts with the intermediate-stage grain size. A similar approach was made in a previous study on “Zpex Smile” Tosoh zirconia, where the initial particle size could not be used in the model because of the presintering of reactive nanograins [28]. The modelling of the sintering trajectory is shown in Figure 8b. The modelled trajectories correspond well with the final relative density and grain size determined experimentally. The error was less than 4% for the final grain size and approximately 1% for the final relative density.

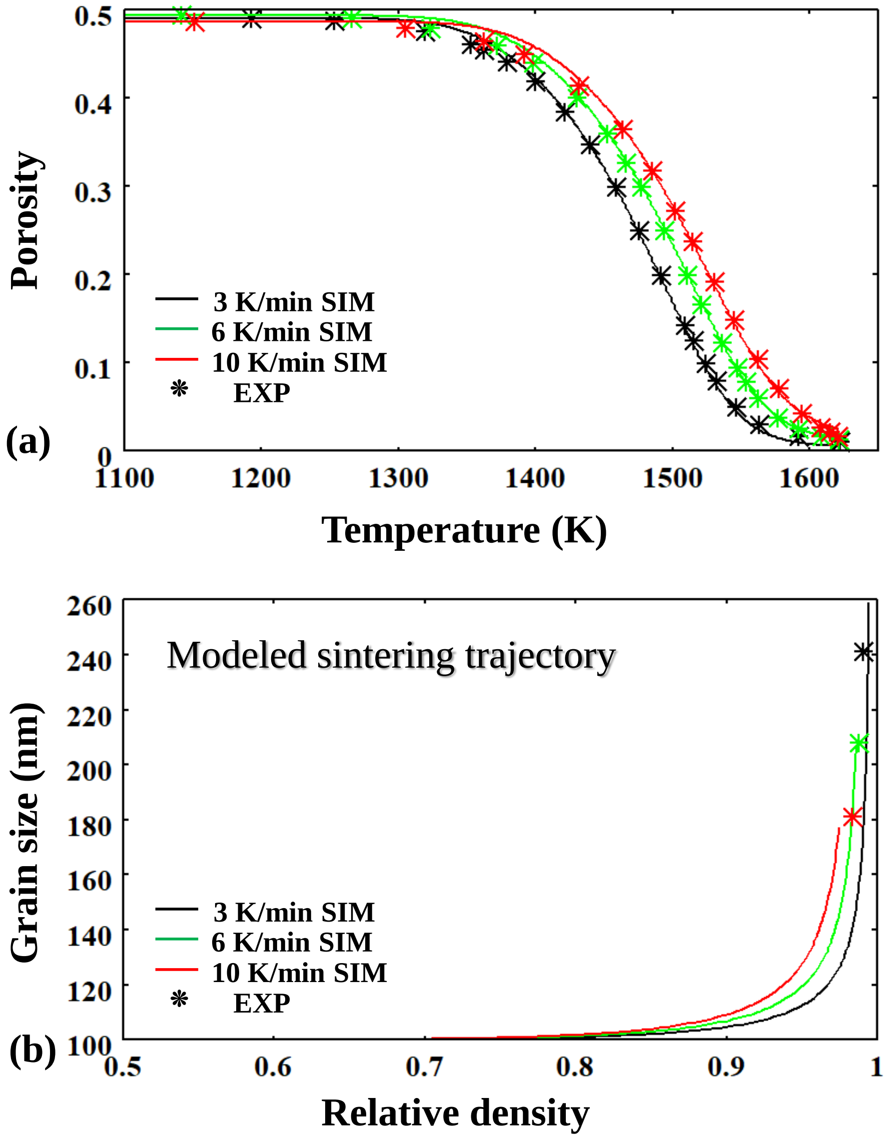

Figure 8 Analytic sintering model with grain growth, (a) modelling of the relative density curves and (b) modelling of the sintering trajectory curves; see electronic version for the colour artwork.

5. Conclusions

In this work, the grain growth exhibited during the final stage of sintering was predicted based on shrinkage data rather than SEM analysis of interrupted sintering. This was carried out by calculating the grain size evolution required to explain the reduction in the densification rate during the final stage. This approach was applied to a master sintering curve allowing densification and grain growth to be modelled with high accuracy. One advantage of this method is that the activation energy can be determined independently of the master sintering curve to adjust the bulk modulus *via* a direct regression method. Consequently, this method is less influenced by theoretically determined porosity functions (i.e., bulk modulus). During the initial stage, presintering of the nanoparticles was revealed using a grain growth estimation method. This phenomenon was found to take place in the region 1200–1350 K; it implies a very limited densification but a rapid stabilisation of the average grain size at approximately 100 nm. Grain growth was estimated from shrinkage *via* two sintering models for each experiment generating two possible grain growth curves based on lattice-diffusion or grain–boundary-diffusion mechanisms. These two curves were relatively dissimilar but converged to a unique sintering trajectory that corresponded well with the experimentally-determined trend.

The main advantage of the method presented in this study is that it combines the simplicity of a master sintering curve study with the optimum extraction of all the main modelling parameters (viscosity, modulus, and grain growth).

Acknowledgements

The authors would like to thank Jérome Lecourt and Christelle Bilot for their help with this study. We would like to thank the French Ministry of Research and Thalès Alenia Space for the PhD grant awarded to Thomas Grippi. The project region normadie - 00016601-20E02057_RIN RECHERCHE 2020 - Emergent – ULTIMODULUS support this study.

Data availability

Experimental data from this study are available from the corresponding author upon reasonable request.

Declaration of Competing Interest

The authors declare that they have no known competing financial interests or personal relationships that could have appeared to influence the work reported in this paper.

Conflict of Interest

The authors declare no conflict of interest.

Credit authorship contribution statement

Charles Manière: Conceptualisation, Supervision, Modelling, Writing; **Thomas Grippi:** Experimentation, Conceptualisation; **Sylvain Marinel:** Conceptualisation, Supervision, Reviewing, and Editing.

References

[1] R.K. Bordia, S.-J.L. Kang, E.A. Olevsky, Current understanding and future research directions at the onset of the next century of sintering science and technology, J. Am. Ceram. Soc. 100 (2017) 2314–2352. doi:10.1111/jace.14919.

[2] J. Zhao, M.P. Harmer, Effect of Pore Distribution on Microstructure Development: III,

Model Experiments, J. Am. Ceram. Soc. 75 (1992) 830–843. doi:10.1111/j.1151-2916.1992.tb04148.x.

[3] M.N. Rahaman, Sintering of Ceramics, CRC Press, 2007.

[4] R.M. German, Sintering Theory and Practice, Wiley, Wiley, 1996. http://www.wiley.com/WileyCDA/WileyTitle/productCd-047105786X.html.

[5] R.L. Coble, Initial Sintering of Alumina and Hematite, J. Am. Ceram. Soc. 41 (1958) 55–62. doi:10.1111/j.1151-2916.1958.tb13519.x.

[6] R.L. Coble, Sintering Crystalline Solids. I. Intermediate and Final State Diffusion Models, J. Appl. Phys. 32 (1961) 787–792. doi:10.1063/1.1736107.

[7] R.L. Coble, Sintering Crystalline Solids. II. Experimental Test of Diffusion Models in Powder Compacts, J. Appl. Phys. 32 (1961) 793–799. doi:10.1063/1.1736108.

[8] J.D. Hansen, R.P. Rusin, M.-H. Teng, D.L. Johnson, Combined-Stage Sintering Model, J. Am. Ceram. Soc. 75 (1992) 1129–1135. doi:10.1111/j.1151-2916.1992.tb05549.x.

[9] J. Wang, R. Raj, Estimate of the Activation Energies for Boundary Diffusion from Rate-Controlled Sintering of Pure Alumina, and Alumina Doped with Zirconia or Titania, J. Am. Ceram. Soc. 73 (1990) 1172–1175. doi:10.1111/j.1151-2916.1990.tb05175.x.

[10] H. Su, D.L. Johnson, Master Sintering Curve: A Practical Approach to Sintering, J. Am. Ceram. Soc. 79 (1996) 3211–3217. doi:10.1111/j.1151-2916.1996.tb08097.x.

[11] W.S. Young, I.B. Cutler, Initial Sintering with Constant Rates of Heating, J. Am. Ceram. Soc. 53 (1970) 659–663. doi:10.1111/j.1151-2916.1970.tb12036.x.

[12] S.J. Park, P. Suri, E. Olevsky, R.M. German, Master Sintering Curve Formulated from Constitutive Models, J. Am. Ceram. Soc. 92 (2009) 1410–1413. doi:10.1111/j.1551-2916.2009.02983.x.

[13] S.J. Park, S.H. Chung, J.M. Martín, J.L. Johnson, R.M. German, Master Sintering Curve for Densification Derived from a Constitutive Equation with Consideration of Grain Growth: Application to Tungsten Heavy Alloys, Metall. Mater. Trans. A. 39 (2008) 2941–2948. doi:10.1007/s11661-008-9654-7.

[14] G. Kerbart, C. Manière, C. Harnois, S. Marinel, Master sintering curve with dissimilar grain growth trajectories: A case study on MgAl2O4, J. Eur. Ceram. Soc. 41 (2021) 1048–1051. doi:10.1016/j.jeurceramsoc.2020.09.003.

[15] A. Talimian, V. Pouchly, H.F. El-Maghraby, K. Maca, D. Galusek, Impact of high energy ball milling on densification behaviour of magnesium aluminate spinel evaluated by master sintering curve and constant rate of heating approach, Ceram. Int. 45 (2019) 23467–23474. doi:10.1016/j.ceramint.2019.08.051.

[16] R. Bollina, S.J. Park, R.M. German, Master sintering curve concepts applied to full-density supersolidus liquid phase sintering of 316L stainless steel powder, Powder Metall. 53 (2010) 20–26. doi:10.1179/174329009X409688.

[17] X. Song, J. Lu, T. Zhang, J. Ma, Two-Stage Master Sintering Curve Approach to Sintering Kinetics of Undoped and Al2O3-Doped 8 Mol% Yttria-Stabilized Cubic Zirconia, J. Am. Ceram. Soc. 94 (2011) 1053–1059. doi:10.1111/j.1551-2916.2010.04199.x.

[18] C. Manière, E.A. Olevsky, Porosity dependence of powder compaction constitutive parameters: Determination based on spark plasma sintering tests, Scr. Mater. 141 (2017) 62–66. doi:10.1016/j.scriptamat.2017.07.026.

[19] C. Manière, C. Harnois, S. Marinel, Porous stage assessment of pressure assisted sintering modeling parameters: a ceramic identification method insensitive to final stage grain growth disturbance, Acta Mater. 211 (2021) 116899. doi:10.1016/j.actamat.2021.116899.

[20] E.A. Olevsky, Theory of sintering: from discrete to continuum, Mater. Sci. Eng. R Reports. 23 (1998) 41–100. doi:10.1016/S0927-796X(98)00009-6.

[21] V.V. Skorohod, Rheological basis of the theory of sintering, Nauk. Dumka, Kiev. (1972).

[22] C. Manière, L. Durand, A. Weibel, C. Estournès, A predictive model to reflect the final stage of spark plasma sintering of submicronic α-alumina, Ceram. Int. 42 (2016) 9274–9277. doi:10.1016/j.ceramint.2016.02.048.

[23] G. Kerbart, C. Manière, C. Harnois, S. Marinel, Predicting final stage sintering grain growth affected by porosity, Appl. Mater. Today. 20 (2020) 100759. doi:10.1016/j.apmt.2020.100759.

[24] G. Bernard-Granger, C. Guizard, Spark plasma sintering of a commercially available granulated zirconia powder: I. Sintering path and hypotheses about the mechanism(s) controlling densification, Acta Mater. 55 (2007) 3493–3504. doi:10.1016/j.actamat.2007.01.048.

[25] C. Manière, E. Saccardo, G. Lee, J. McKittrick, A. Molinari, E.A. Olevsky, Swelling negation during sintering of sterling silver: An experimental and theoretical approach, Results Phys. 11 (2018) 79–84. doi:10.1016/j.rinp.2018.08.035.

[26] C. Manière, L. Durand, G. Chevallier, C. Estournès, A spark plasma sintering densification modeling approach: from polymer, metals to ceramics, J. Mater. Sci. 53 (2018) 7869–7876. doi:10.1007/s10853-018-2096-8.

[27] C. Manière, S. Chan, G. Lee, J. McKittrick, E.A. Olevsky, Sintering dilatometry based grain growth assessment, Results Phys. 10 (2018) 91–93. doi:10.1016/j.rinp.2018.05.014.

[28] C. Manière, G. Lee, J. McKittrick, S. Chan, E.A. Olevsky, Modeling zirconia sintering trajectory for obtaining translucent submicronic ceramics for dental implant applications, Acta Mater. 188 (2020) 101–107. doi:10.1016/j.actamat.2020.01.061.

[29] C. Manière, L. Durand, A. Weibel, C. Estournès, Spark-plasma-sintering and finite element method: From the identification of the sintering parameters of a submicronic α -alumina powder to the development of complex shapes, Acta Mater. 102 (2016) 169–175. doi:10.1016/j.actamat.2015.09.003.

[30] J.A. Alvarado-Contreras, E.A. Olevsky, R.M. German, Modeling of gravity-induced shape distortions during sintering of cylindrical specimens, Mech. Res. Commun. 50 (2013) 8–11. doi:10.1016/j.mechrescom.2013.02.007.

[31] J. Besson, M. Abouaf, Grain growth enhancement in alumina during hot isostatic pressing, Acta Metall. Mater. 39 (1991) 2225–2234. doi:10.1016/0956-7151(91)90004-K.

[32] Z.-Z. Du, A.C.F. Cocks, Constitutive models for the sintering of ceramic components—I. Material models, Acta Metall. Mater. 40 (1992) 1969–1979. doi:10.1016/0956-7151(92)90183-F.

[33] E.A. Olevsky, C. Garcia-Cardona, W.L. Bradbury, C.D. Haines, D.G. Martin, D. Kapoor, Fundamental Aspects of Spark Plasma Sintering: II. Finite Element Analysis of Scalability, J. Am. Ceram. Soc. 95 (2012) 2414–2422. doi:10.1111/j.1551-2916.2012.05096.x.

[34] M.I. Mendelson, Average Grain Size in Polycrystalline Ceramics, J. Am. Ceram. Soc. 52 (1969) 443–446. doi:10.1111/j.1151-2916.1969.tb11975.x.

[35] M. Abouaf, J.L. Chenot, G. Raisson, P. Bauduin, Finite element simulation of hot

isostatic pressing of metal powders, Int. J. Numer. Methods Eng. 25 (1988) 191–212. doi:10.1002/nme.1620250116.

[36] C. Manière, G. Kerbart, C. Harnois, S. Marinel, Modeling sintering anisotropy in ceramic stereolithography of silica, Acta Mater. 182 (2020) 163–171. doi:10.1016/j.actamat.2019.10.032.

[37] A. Borrell, M.D. Salvador, E. Rayón, F.L. Peñaranda-Foix, Improvement of microstructural properties of 3Y-TZP materials by conventional and non-conventional sintering techniques, Ceram. Int. 38 (2012) 39–43. doi:10.1016/j.ceramint.2011.06.035.

[38] M. Mazaheri, A. Simchi, M. Dourandish, F. Golestani-Fard, Master sintering curves of a nanoscale 3Y-TZP powder compacts, Ceram. Int. 35 (2009) 547–554. doi:10.1016/j.ceramint.2008.01.008.

[39] E. Yamalaç, Sintering, Co-sintering and Microstructure Control of Oxide based Materials : Zirconia, Alumina, Spinel, Alumina-Zirconia and Spinel-Alumina, PhD, Genoble University and Izmir Institute of Technology, 2010. https://tel.archives-ouvertes.fr/tel-00521852.

[40] L.S. Arias-Maya, Free and constrained sintering of 3-mol % yttria stabilised zirconia, DYNA. 81 (2014) 158. doi:10.15446/dyna.v81n183.36918.

[41] V. Pouchly, K. Maca, Master sintering curve: A practical approach to its construction, Sci. Sinter. 42 (2010) 25–32. doi:10.2298/SOS1001025P.

[42] V. Pouchly, K. Maca, Z. Shen, Two-stage master sintering curve applied to two-step sintering of oxide ceramics, J. Eur. Ceram. Soc. 33 (2013) 2275–2283. doi:10.1016/j.jeurceramsoc.2013.01.020.

[43] H.A. Tajiri, H.A. Al-Qureshi, Manufacturing and characterization of porous ceramic capillary membranes for enzyme functionalization through click chemistry, J. Brazilian Soc. Mech. Sci. Eng. 42 (2020) 170. doi:10.1007/s40430-020-2254-1.

[44] H. Majidi, T.B. Holland, K. van Benthem, Quantitative analysis for in situ sintering of 3% yttria-stablized zirconia in the transmission electron microscope, Ultramicroscopy. 152 (2015) 35–43. doi:10.1016/j.ultramic.2014.12.011.

[45] Y. Dong, L. Qi, J. Li, I.-W. Chen, A computational study of yttria-stabilized zirconia: II. Cation diffusion, Acta Mater. 126 (2017) 438–450. doi:10.1016/j.actamat.2017.01.008.

[46] R. Chaim, Activation energy and grain growth in nanocrystalline Y-TZP ceramics,

Mater. Sci. Eng. A. 486 (2008) 439–446. doi:10.1016/j.msea.2007.09.022.

[47] Y. Dong, H. Wang, I.-W. Chen, Electrical and hydrogen reduction enhances kinetics in doped zirconia and ceria: I. grain growth study, J. Am. Ceram. Soc. 100 (2017) 876–886. doi:10.1111/jace.14615.

Figure captions

Figure 1 Skorohod’s bulk modulus (black) and corrected moduli including initial stage critical porosity (green curve) and both initial, final stages critical porosities (red curve).

Figure 2 Relative density curves at constant heating rate of 3, 6 and 10 K/min.

Figure 3 Sintering activation energy identification via the master sintering curve (a) and the method developed by Wang and Raj (b).

Figure 4 Modelling of the intermediate stage of sintering by direct regression using the MSC-derived activation energy (a); adjustment of the bulk modulus by critical porosity of the initial stage (b); analytical modelling of the porosity without grain growth (c); see electronic version for the colour artwork.

Figure 5 Final microstructures of samples sintered at 10 K/min (a), 6 K/min (b), 3 K/min (c).

Figure 6 Estimated grain size as a function of temperature. G LD refers to the grain size curve corresponding to a lattice-diffusion mechanism, and G GBD refers to that corresponding to a grain–boundary-diffusion mechanism; see electronic version for the colour artwork.

Figure 7 Predicted sintering trajectories based on estimated grain-size curves (a), identification of grain growth model based on the 3 K/min grain-boundary-diffusion-controlled sintering trajectory curve (b) ; see electronic version for the colour artwork.

Figure 8 Analytic sintering model with grain growth, (a) modelling of the relative density curves and (b) modelling of the sintering trajectory curves; see electronic version for the colour artwork.

Table caption

Table 1 Interrupted sintering grain growth study at 3 K/min